TUDelft

Delft University of Technology

On Wind Turbine structural stiffness influence on wake flow

Muscari, C.; Giordani, R.; Schito, P.

Important note
To cite this publication, please use the final published version (if applicable).
Please check the document version above.

On Wind Turbine structural stiffness influence on wake flow

C. Muscari [a,b,*], R. Giordani [a], P. Schito [a]

[a] *Politecnico di Milano, Milano, Italy*
[b] *TU Delft, Delft, Netherlands*

ARTICLE INFO

ABSTRACT

In this work we test a Fluid–Structure Interaction (FSI) method based on the SOWFA+ OpenFAST framework. The linear structural module of FAST is coupled to SOWFA's Actuator Line simulations to perform the aeroelastic analysis of a wind tunnel scaled model (1:75) of the DTU 10 MW turbine. The objective is to give a quantitative description of the turbine stiffness influence on the wake flow by varying the model structural properties.

The simulations are performed in two different operating conditions: below rated ($TSR = 7.5$) and above rated ($TSR = 5.5$). Turbulence is generated by positioning disturbing elements at the inlet, analogously to what was done in the reference wind tunnel tests. Results show that flexibility starts to have a considerable impact on the wake velocity deficit when the tip deflection is somewhere between 4% and 12% of the blade length.

Based on these results, an indication is given of when the accuracy obtainable with the CFD-CSD coupling justifies the increased computational cost.

1. Introduction

In 2014, the European Union set a legally binding target to 2030 for at least 27% of the energy consumed in Europe to be coming from renewable sources, and wind energy currently leads the way in reaching this very ambitious goal. A key driver, in this research field, is the LCOE (Levelised Cost of Energy) minimization. The most obvious way to reduce it at a wind turbine level is to increase blade size, which, of course, affects flexibility. The main consequence is the coupling of the considerable deflections with the unsteady aerodynamic loads as documented in Ahlström (2006).

Although aeroelastic stability has typically not been a key design driver for rotor blades up to now, the situation might change for future highly flexible and large rotors.

The turbines of the future are not only bigger but also installed closer and closer together. At a wind farm level, an accurate enough modeling of wake dynamics is necessary to optimize layout, operation, and control. Wake dynamics and rotor aeroelasticity are strongly coupled and influence each other in a complex way that the simple analytical models often used to describe one or the other cannot account for.

Current aerodynamic theories do not accurately describe the interaction between a highly variable inflow and the unsteady aerodynamics of the moving and deforming blades. Blades moving through air shed vorticity, normally convected downstream and away from a relatively stiff structure. When the blades flex out-of-plane, the rotor interacts with its vorticity, calling the design assumptions' accuracy into question. Additionally, structural dynamics of blades incorporating

* Corresponding author at: Politecnico di Milano, Milano, Italy.
  E-mail address: claudia.muscari@polimi.it (C. Muscari).

composite materials, built-in curvature and sweep, and large non-linear deflection (including torsion and bend-twist coupling) further complicate the physics and the assessment of stability.

Recently, Fluid–Structure Interaction (FSI) frameworks which contain an aerodynamic part that determines the wind loads and a structural part to describe the dynamic response of the structure, gained much interest. At the high fidelity extreme of the FSI spectrum, we find CFD-CSD (Computational Fluid Dynamics and Computational Structural Dynamics) methods. In Hsu and Bazilevs (2012) the FSI framework consisted of a low-order Arbitrary Lagrangian-Eulerian Variational Multi-Scale (ALE-VMS) flow solver and modeling of the rotor blades as thin composite shells. Results were obtained for a single blade. Yu and Kwon (2014) combined an unstructured mesh CFD solver and a FEM-based CSD solver to predict unsteady aerodynamic loads and aeroelastic deformations. More recently, Sayed et al. (2019) presented an explicit coupling between a URANS solver and a structural solver based on non-linear Timoshenko beam elements. Their results showed an increase of rotor power and thrust by 1% and 0.3%, respectively, due to the large edgewise deformation that significantly increases the contribution of the radial force to the total torque of the turbine. None of these studies explicitly focused on the wake, although the information on thrust variation (going from rigid to flexible model) given by Sayed et al. (2019) for a 180 m diameter wind turbine gives us an idea of the numbers we are dealing with (thrust force and wake development are strongly related). Finally, in Ma et al. (2019) an effort in this direction is made by developing a low computational cost method combining the Actuator Line Model (ALM) and finite-element beam theory and using it to study velocity and vorticity distribution in the far wake. They conclude that neglecting blade flexibility leads to a slight underestimation of velocity recovery and that no appreciable improvements were attained when considering non-linear effects. In Rodriguez et al. (2021) the stability of tip vortices shed from flexible rotors is studied with an aeroelastic free-vortex wake method. The main results were the validation of their framework and the observation that the wakes of flexible rotors experience an early breakdown due to an initial transient of flapwise deflection and are not influenced by the torsional response.

A big limitation of all the presented studies was that the used frameworks were not validated on experimental data (which is poor or nonexistent for big rotors) and that, even though all the used methods are very computationally expensive, no clear indication as to when their use is essential was given.

Our study aims at addressing the latter issue by introducing flexibility effects not by considering a big rotor but rather by changing the structural properties of the blade. We considered the scaled model of the DTU 10 MW turbine described in Bak et al. (2013) and tested three structural models in two different operating conditions under turbulent inflow.

The study is outlined as follows. The applied methodology for both the aerodynamic and the structural part is discussed in Section 2. The turbine and the data are described in Section 3. Finally, after discussing the Numerical Setup and the Inflow in Sections 4 and 4.3.1, the results are presented and discussed in Section 5, where we also elaborate on the consequences of neglecting non-linear effects.

2. Methods

This section presents and discusses the adopted models for the aerodynamic and structural parts. For both, there will be a theoretical introduction first and then a description of the software. The aerodynamic part is dealt with using the actuator line model, the go-to strategy for high-fidelity wind turbine modeling. For the structural part, an Euler–Bernoulli beam model will be used.

2.1. Aerodynamic model

The Actuator Line Model (ALM), Sørensen and Shen (2002), descends directly from the BEM (Blade Element Momentum) method. The turbine does not physically exist in the domain but is modeled by computing the forces through tabulated data or an aeroelastic code and then directly introduced as body forces in the Navier Stokes equations. The ALM represents each blade as a radially varying force line. The actuator line is discretized by means of a number of points. For each point the so-called free-stream velocity is sampled and velocity magnitude and angle of attack are computed. The lift and drag coefficients are determined from airfoil data and used to calculated the forces which have to be corrected for 3D effects. A popular correction (Shen et al., 2005) is based on the Glauert formulation, which multiplies the forces of each blade section by a function F_{tip}, based on the local section radius r.

$$F_{tip} = \frac{2}{\pi} cos^{-1} \left(e^{-g \frac{B(R_{tip}-r)}{2r sin(|\phi|)}} \right) \tag{1}$$

where B is the number of blades, R_{tip} is the tip radius, ϕ is the flow angle, and g is an empirical correction function. In order to apply the correction to the root, a very similar equation is used:

$$F_{root} = \frac{2}{\pi} cos^{-1} \left(e^{-g \frac{B(r-R_{root})}{2r sin(|\phi|)}} \right) \tag{2}$$

where R_{root} is the root radius. In practical terms, F_{tip} and F_{root} reduce the forces on blade sections to zero at the tip and root, while having small effects near the blade center.

The force per unit volume is calculated and inserted as a source term in the NS equations for the corresponding cell:

$$\vec{f} = \frac{\vec{L} + \vec{D}}{V_{cell}} \tag{3}$$

where L and D are the blade point lift and drag and V_{cell} is the volume of the cell containing the blade point. Since the blade surface is not modeled, the model does not replicate finer flow features such as the boundary layer and the separation at high angles of attack. However, the wake development and interaction with the atmospheric boundary layer can be captured, resolving the turbulent eddies up to the blade chord scale. Two crucial aspects of the AL that differentiate the many AL models available are:

- the free-stream velocity sampling;
- the projection of the body force.

The free-stream velocity's correct definition, although not straightforward, is fundamental to obtaining accurate results. The projection issue concerns how the computed body forces are applied back to the domain. The most physical solution would be to apply them in the singular cell containing the airfoil pressure center, but, mathematically speaking, this could be very problematic since the sharp gradient generated could lead to strong spurious oscillations in the actuator line vicinity. The solution is to apply some kind of smearing function to distribute the force in multiple cells avoiding the sharp gradients altogether. The one we use for this study was proposed by Sørensen and Shen (2002) and it is a three-dimensional Gaussian function, isotropic in blade width and fixed in width along the blade span.

2.1.1. SOWFA
SOWFA (Simulator fOr Wind Farm Applications) is an open-source extension of OpenFOAM developed by the National Renewable Energy Laboratory (NREL). It is a set of solvers, boundary conditions, and actuator-type turbine models specific for wind farm applications. SOWFA allows the reproduction of a range of different atmospheric conditions, and the wind turbine wakes and the interaction between them. Further information can be found in Churchfield et al. (2012).

2.2. Structural model

Structural models used in aeroelastic modeling of wind turbine blades can be roughly categorized into 3D FEM and 1D equivalent models. The 1D beam model is much faster than 3D FEM and provides accurate results if appropriately constructed. Wind turbines are slender structures having one principal dimension much larger than the other two. Therefore, they can be efficiently modeled using 1D models. The beam axis is defined along the span-wise direction, and a cross-section perpendicular to this axis varies along the span. The beam models can be divided into linear and non-linear models. A very comprehensive review on this topic can be found in Hansen et al. (2006). This study is mainly performed with a linear model. This is mainly motivated by the fact that the non-linear structural module of OpenFAST is not integrated in the coupling. However, some considerations on that regard are presented at the end of Section 5.

The most used linear beam model is the Euler–Bernoulli beam model. The blade is modeled as a flexible cantilever beam with distributed mass and stiffness. The slender beam is subjected to extensional, torsional and bending loads, neglecting the shear deformations. In the modal approach, the flexible bodies' deflection shape is described as a linear combination of a set of modes shapes, which are usually obtained from a finite element pre-processor. Following Jonkman (2003), at any point on the structural element, the lateral deformation can be expressed as

$$u(z, t) = \sum_{i=1}^{n} \phi_i(z) q_i(t) \tag{4}$$

where ϕ_i and q_i are the normal mode shape and the generalized coordinate of the ith normal mode.

Alternatively, these deflections could be expressed using n other functions, $\varphi_j(z)$, not unique to each normal mode:

$$u(z, t) = \sum_{j=m}^{n+m-1} \varphi_j(z) q_j(t) \tag{5}$$

According to the Rayleigh–Ritz method, each normal mode shape can be obtained combining the n shapes functions with the constant proportionality coefficient $C_{i,j}$:

$$\phi_i = \sum_{j=m}^{n+m-1} C_{i,j} \varphi_j \tag{6}$$

The linear structural solver used in this work considers polynomial shape functions:

$$\varphi_j(z) = \left(\frac{z}{Z}\right)^j \tag{7}$$

The coefficients $C_{i,j}$ can be found by solving:

$$(-\omega_i^2 \underline{\underline{M}} + \underline{\underline{K}})\underline{C_i} = \underline{0} \tag{8}$$

where $\underline{\underline{M}}$ and $\underline{\underline{K}}$ are the $n \times n$ mass and stiffness matrix, respectively. ω_i is the ith natural frequency.

The normal mode superposition is an effective way to reduce the degrees of freedom and, therefore, reduce the problem's size. However, the modal approach's flexibility is restricted by the type and number of DOFs allowed in the structure, leaving aside the possibility to include the torsional eigenmodes.

2.2.1. OpenFAST

OpenFAST is the latest version of FAST (Fatigue, Aerodynamics, Structures, and Turbulence), a multi-physics, multi-fidelity tool for simulating coupled dynamic response of wind turbines developed at NREL. In Jonkman et al. (2005), its use and code structure are detailed. It is a framework written in Fortran 2003 that couples computational modules for aerodynamics, hydro-dynamics for offshore structures, control and electrical system dynamics, and structural dynamics to enable coupled non-linear aero-hydro-servo-elastic simulation in the time domain. It can simulate a variety of wind turbine configurations, both onshore and offshore, taking into account numerous physical phenomena. The modules used in this study are:

- **AeroDyn**, the aerodynamic module that enables the aeroelastic simulation on both the tower and the blades. It can run in BEM method mode or in the coupled mode with SOWFA. When coupled with SOWFA, this module performs the blade element part of the BEM, while the momentum part is performed by the CFD software, as already explained.
- **InflowDyn**, is the module that provides the wind inflow information to AeroDyn. When OpenFAST is coupled with the CFD software, it is replaced by SOWFA.
- **ElastoDyn**, the linear structural-dynamics module. It is based on the modal approach. It takes the aerodynamic loads as input and returns the accelerations, the velocities, and the reaction loads of the wind turbine. It allows the user to activate up to 24 degrees of freedom.
- **BeamDyn**, the non-linear time-domain structural-dynamics module based on GEBT (Geometrically Exact Beam Theory). It supports the full geometric non-linearities and large deflection with bending, torsion, shear, extensional degree of freedom. It takes the complete mass and stiffness matrices as input to model anisotropic composite materials, twisted and pre-coned configurations.

2.3. Coupling

When SOWFA runs coupled with OpenFAST, the blade element theory calculations are performed by its AeroDyn module. The actuator line CFD model replaces the momentum part of BEM. For this reason, the two software continually exchange information, and a typical run follows the steps below:

1. SOWFA feeds OpenFAST inflow information at blade elements;
2. The aerodynamic forces are computed by look-up table;
3. OpenFAST computes the turbine structural and system response;
4. The modified aerodynamic forces are fed back to the CFD.

When the ElastoDyn and BeamDyn modules are also active in FAST, the fed-back forces also account for the blade deflection.

3. The model turbine and the experimental data

This section describes the model turbine considered for the study and the experimental data that will be used for comparison.

3.1. The turbine

The chosen turbine is the (1:75) scaled model of the DTU 10 MW wind turbine that was developed during the H2020 project Life50+ by Bayati et al. (2016). The scaling parameters reflect the desire of finding an optimal compromise between maximizing the dimensions for lowering the Reynolds mismatch and limiting the dimensions to limit the blockage ratio, around 8%. The main characteristics of the turbine are gathered in Table 1.

3.1.1. Aerodynamic characteristics

The aerodynamic design has been carried out with the aim of matching the reference thrust and torque coefficients, the scaled first blade flap-wise frequency, and the correct blade weight. In order to reach these goals, the PoliMi model uses completely different airfoils, twist and chord distributions.

Table 1
Turbine characteristics.

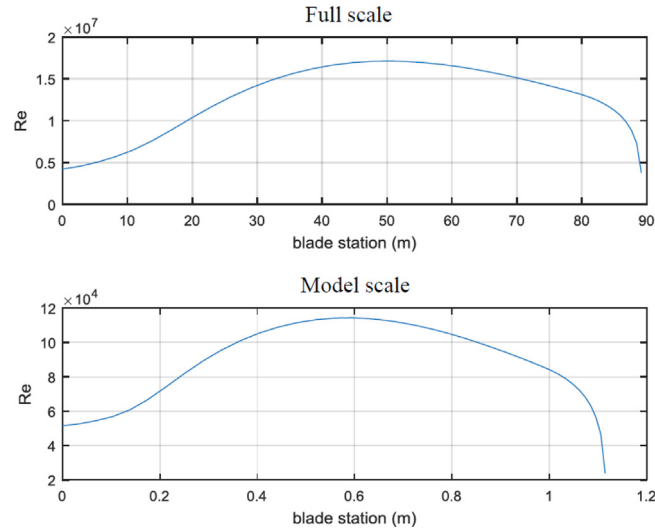| Blade number	3
Diameter	2.38 m
Tower height	1.98 m
Shaft Tilt	$-5°$

Fig. 1. Reynolds number distribution for the full scale DTU 10 MW and for the scaled model.
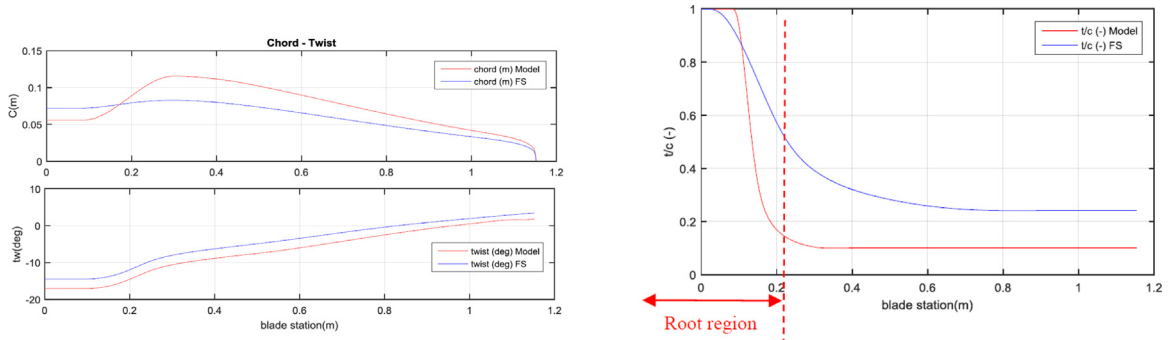

Fig. 2. Chord, twist and thickness distributions for the full scale DTU 10 MW (FS) and for the scaled model.

Airfoil geometry. The Reynolds number obtainable in the wind tunnel impose the choice of different airfoils along the blade with respect to the full scale model, as shown in Fig. 1. In order to match the aerodynamic performance at lower Reynolds numbers, the entire blade is designed using the SD7032 airfoil. Only the area near the blade root the blade section shape is interpolated with the circular section thus allowing a smooth transition to the circular blade root section.

Blade geometry. The scaled model chord and twist distributions are different from the full scale one. The chord has been changed to match the scaled rotor thrust, whether the twist has been designed taking into account the different zero lift value of the airfoil used. Chord, twist and thickness distributions along the blade for the two models are shown in Fig. 2.

3.1.2. Structural characteristics

The wind tunnel model has been designed to study both aerodynamic and aeroelastic performances. Therefore, a proper structural scaling has been taken into account. The resulting wind turbine can be used to conduct aeroelastic researches as it is the main goal of this work.

The blade has been built with a single high modulus carbon fiber layer of 0.3 mm thickness in order to match the mass target and preserve the high stiffness required. The first flap-wise frequency is around 15 Hz, approximately the value required to preserve the structural characteristics of the full scale turbine.

Table 2
Operational parameters.

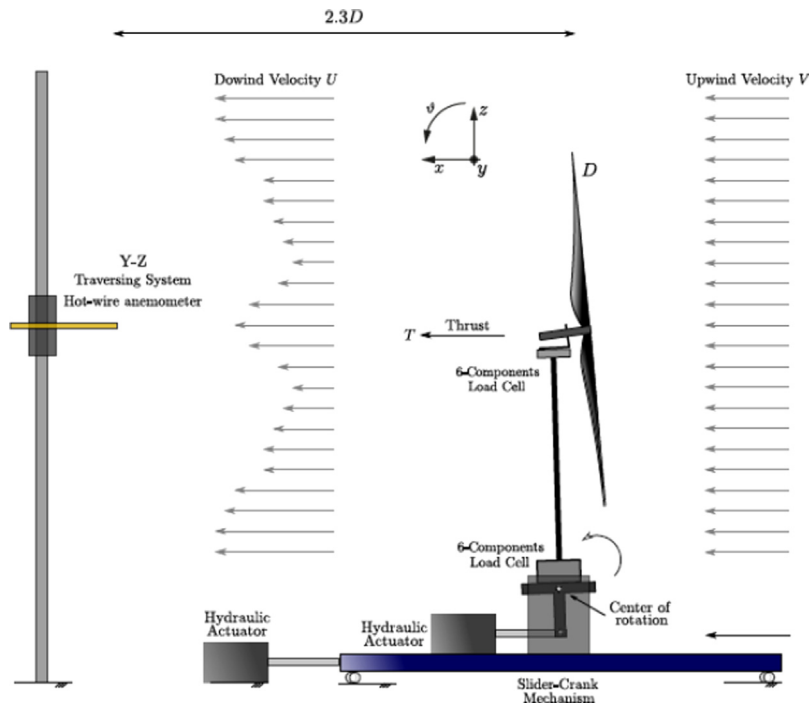| Condition	Wind speed	Rotor speed	TSR	Pitch angle
Rated 2	4.0 m/s	241 rpm	7.5	0°
Above rated	6.0 m/s	265 rpm	5.5	12.5°

Fig. 3. Experimental measurement system setup.
Source: From Bayati et al. (2018).

The tower is a 1.54 m long pole of constant cylindrical cross section. It is made up by carbon fiber, resulting very light and stiff, being its first natural frequency around 11 Hz. The model is built in carbon fiber which provides the best compromise between mass density and stiffness.

3.2. The experimental data

The considered experimental data was obtained during the UNAFLOW project 2018. The test campaign has been carried out in the PoliMi Wind Tunnel boundary layer section. The section has a 36 m length, 14 m width and 4 m height, allowing for very low blockage effects in the tests. The operational parameters reported in Table 2 were considered. Rotor speed and collective pitch angle were fixed. At Rated 2, the wind turbine is operated at the optimum full-scale value of tip-speed ratio (TSR), and the power coefficient is the maximum one. In the above-rated condition the TSR is lower and the collective pitch angle is increased, to preserve rated power. Experiments were carried out in smooth flow, and the turbulence intensity across the test section height was approximately 2%.

Several quantities were measured during the experiments. The undisturbed wind velocity was measured by a pitot tube 7.15 m upstream of the rotor at hub height. The tower-top forces were measured by a six-component force transducer. In a few selected test cases, the wake of the wind turbine was scanned by triaxial hot-wire probes. In an even smaller sample of test cases, PIV measurements were carried out to describe the wake flow structure. The absence of sensors on the blades limits our analysis to a comparison of the wake. The measurements of the velocity in the wake provided for the comparison in this study, refer to the condition that in Table 2 is called *Rated2*. The experimental measurement system setup is shown in Fig. 3.

The thrust coefficient has been provided as a function of the tip-speed ratio to consider different conditions in the simulations.
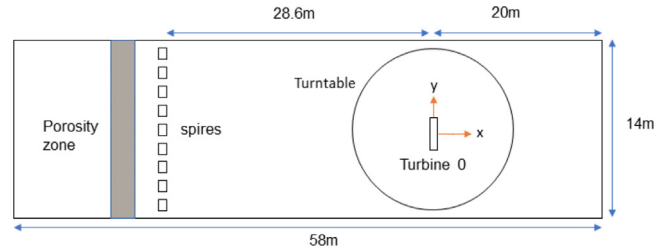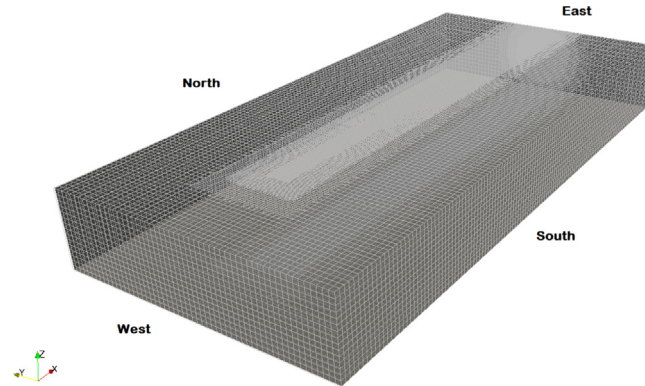
Fig. 4. Numerical wind tunnel configuration.

Fig. 5. Mesh layout and patches.

4. Numerical setup

This section is about the case setup. Section 4.1 describes the domain and its discretization, then in 4.2, 4.3 and 4.4 the choices in terms of time step, boundary conditions and numerics are justified.

4.1. Space discretization

The considered computational domain is 14 m wide, 3.8 m high, and 58 m long, with the reference system located 10 rotor diameters downstream of the inlet, at the turbine location. The length has been increased from the 35 m of the actual wind tunnel to 58 m to allow a complete turbulence development and to avoid numerical instabilities within the flow. The actuator line does not require a complete description of the blade's geometry, making the mesh simple and composed of only hexahedral cells. The basic mesh is built using the OpenFOAM's *blockMesh* utility, with 464 cells in the streamwise direction, 112 in the cross-stream direction, and 32 in the vertical direction.

SOWFA guidelines indicate that at least 20 cells should cover the rotor diameter to resolve the wake reasonably. Thus, three cylindrical refinement zones extending from some distance upstream of the rotor to the domain end are introduced to better describe the area around the rotor and in the wake. Each refinement split every cell within the selected zone into eight sub-cells. This number allows for a good trade off between accuracy and computational effort. It also makes sense to have a mesh that is increasingly fine going from the far wake to the near wake to the rotor disk. Section 4.5 further details the mesh choice by considering the experimental data. Since we want to consider a turbulent case, we must add turbulence generators inside the domain. The full-scale DTU 10MW model is designed for offshore applications. The wind tunnel configuration that mimics the neutral offshore atmospheric boundary layer uses 14 type-B spires placed side by side 1 m from each other, 1 m downstream of the test chamber inlet. A type-B spire consists of an equilateral trapezoid; its height is 2.0 m, while the widths of the bottom and top edges are 0.26 m and 0.1 m, respectively. Two precursor simulations are performed to analyze the wind turbine in rated and above-rated conditions. The spires described above have been placed 1 m downstream of the porosity zone. The 1 m long porosity zone takes into account the pressure losses within the wind tunnel closed-loop circuit since it is not entirely replicated here. Expressly, the porosity coefficients are set to produce one unit dynamic pressure drop. The spires are modeled through a top-bottom meshing strategy without adding layers around their surfaces. In fact, it is not necessary to accurately resolve their boundary layer if their purpose is just to generate a turbulent flow (see Figs. 4 and 5).

Table 3
Boundary conditions.

Patch	U	p	k	nuSgs
west	fixedValue	zeroGradient	fixedValue	fixedValue
east	inletOutlet	fixedValue	zeroGradient	zeroGradient
lower	uniformFixedValue	zeroGradient	zeroGradient	zeroGradient
upper	uniformFixedValue	zeroGradient	zeroGradient	zeroGradient
north	uniformFixedValue	zeroGradient	zeroGradient	zeroGradient
south	uniformFixedValue	zeroGradient	zeroGradient	zeroGradient

4.2. Time discretization

The time step must be set correctly to avoid numerical instabilities in the simulation both for the fluid model and the structural solver. The structural solver has less strict requirements concerning the CFD since it runs stably up to $\Delta t = 0.01$ s. However, the structural calculation must be performed at least once during a CFD interval, so the same flow time step is used. The parameter used to check the stability of the CFD solution is the Courant Number (CFL), defined as:

$$CFL = \frac{U \Delta t}{\Delta x} \tag{9}$$

Typically, it has to be less than one to prevent the flow from crossing more than one cell every time step. However, scaled wind turbines rotate very fast, so a different definition is introduced:

$$CFL_{tip} = \frac{\omega R \Delta t}{\Delta_g} \tag{10}$$

where ω is the wind turbine rotational speed, R is the blade radius and $\Delta_g = \sqrt[3]{\Delta_x \Delta_y \Delta_z}$ is the equivalent cell dimension. The correct value of this parameter should prevent the tip from crossing more than one cell per time step and guarantee an equal number of force calculations per rotor revolution. In fact, if the time step is too large, the forces can be computed asymmetrically or only in specific positions, introducing oscillations of the loads or vibrations of the structure. A precursor simulation is run for 130 s to stabilize the main flow quantities and have the correct turbine inflow. Velocity and turbulence values reach a quasi-stable condition at around 90 s. The information needed for the successor simulations is gathered starting from 95 s. The time step is set to $\Delta t = 0.001$, maintaining a CFL_{tip} under 2.5 all over the simulation. A small time step is crucial if the intention is to resolve the turbulence field accurately. Further reducing the Δt would require too much CPU time.

4.3. Boundary conditions

The simulation boundary conditions are summarized in Table 3. Two precursor simulations are performed considering different undisturbed velocities at the inlet. Specifically, the values $U_\infty = 3.0$ m/s and $U_\infty = 5.0$ m/s are imposed on the west patch to obtain the desired below-rated and above-rated conditions, respectively. The precursor is an Atmospheric Boundary Layer (ABL) simulation performed on an empty domain to generate initial condition and time-dependent inflow boundary conditions for the main simulation. It should run long enough to generate statistically steady atmospheric turbulence. The hub velocities obtained using these values are around 3.6 m/s for the first case and around 6 m/s for the second case. The above-rated condition differs from that of the experimental test campaign but still represents an above-rated condition. The outlet pressure is set to 0*Pa* (*east patch*). When considering uniform cases, slip condition on the walls is computationally advantageous compared to the no-slip since there is no need to reproduce the wall's viscous effect. Since our case is turbulent, the wind tunnel walls must be modeled, considering the friction they exert on the flow. For this reason we have *uniformFixedValue* conditions. Friction is responsible for the viscous effects near the walls, which generate the turbulence required to match the actual chamber conditions.

4.3.1. Inflow

The atmospheric boundary layer is a complex turbulent flow influenced by many factors. An accurate reproduction of the ABL should match the following characteristics:

- Variation of the wind speed with height;
- Variation of the turbulence intensity with height;
- Variation of the integral scales with height;
- Turbulent spectra coherent with the 5/3 law.

The wind tunnel environment allows generating only a neutral atmospheric boundary layer since the effect of the temperature is not reproduced. Moreover, the flow is confined by the walls, and the complete logarithmic evolution of a real ABL is not obtainable. The simulation of such a turbulent flow inside a wind tunnel is a tedious task and would require
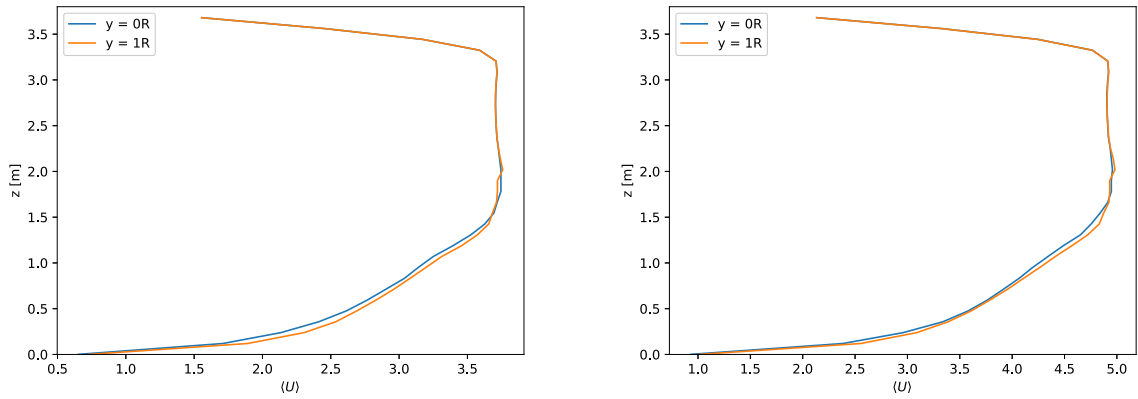
Fig. 6. Mean streamwise velocity profile at vertical coordinates equal to 0 and to the radius - Below (on the left) and Above rated (on the right) condition.
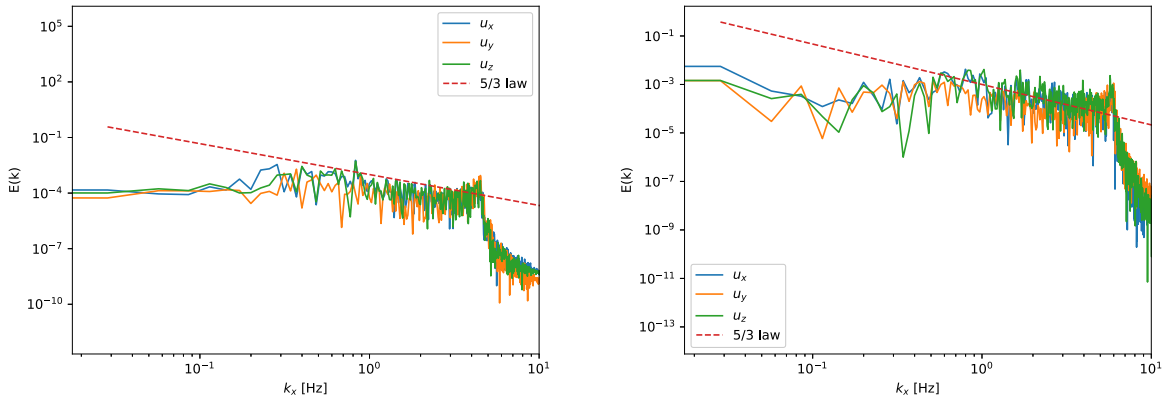

Fig. 7. Energy spectrum at $(x, y, z) = (0, 0, 0)$, rated (on the left) and above rated (on the right) conditions.

further investigation of the CFD parameters. Additionally, the required computational cost is very high, and only a limited time has been reproduced. Further increasing the solution time would probably yield a more developed turbulent flow. Fig. 6 illustrate the mean velocity vertical profile at different lateral positions for the below rated and above rated cases, respectively. The obtained velocity profiles agree with the PoliMi's Wind Tunnel profile for those particular conditions.

The turbulence spectra are reported in Fig. 7. The inertial range follows the "5/3 law" for both cases, indicating a correct simulation of the turbulent field.

4.4. Solver and numerical schemes

The solver used for the simulations is *pisoFoamTurbine.ALMAdvancedOpenFAST*, which was written specifically to perform the coupled simulations and has been validated in various studies (Johlas et al. (2019), Shaler and Jonkman (2021)). The selected force projection is the most common, first defined by Sørensen and Shen (2002): a three-dimensional Gaussian function, isotropic in width and fixed along the blade span. As prescribed by the guidelines, ϵ is set as twice the cell dimension in the rotor area. The PISO loop performs one outer corrector and three inner correctors. The pressure solver used is the preconditioned conjugate gradients (PCB) method with GAMG preconditioner and Preconditioned bi-conjugate gradient (PBiCG) with DILU preconditioner for velocity and turbulence variables.

The discretization schemes used are the *backward* second-order implicit method for the time, second-order unbounded *Gauss linear* for the gradients, and the divergence terms except for the velocity divergence, for which we blend first and second order, and *Gauss linear uncorrected* for the laplacian terms. The laplacian and surface-normal gradient schemes use orthogonality correctors. The turbulence structures are resolved by employing a LES turbulence model with one-equation eddy viscosity SGS model. We also consider porosity with the fixedCoeff model already present in OpenFOAM.

4.5. Experimental data and mesh choice

We performed a comparison between our numerical results and the presented experimental data. The comparison does not constitute a validation of the framework, but it was useful to motivate some of our choices. In particular, when using
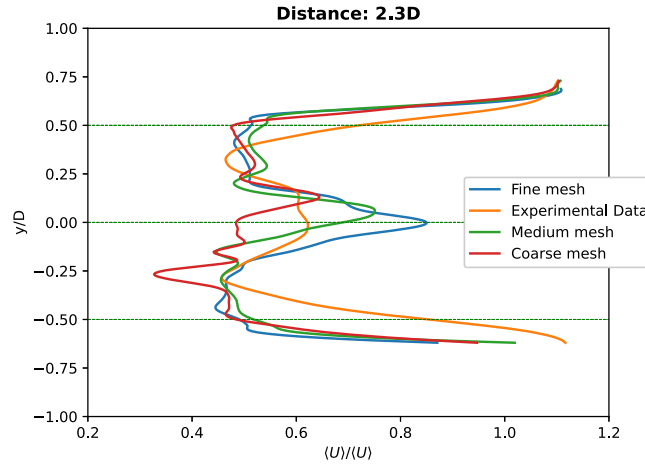
Fig. 8. Streamwise mean velocity horizontal profile.

Table 4
Space discretization.

	Coarse mesh	Intermediate mesh	Fine mesh
Local refinements	2	3	4
Total number of cells	1'140'524	8'689'33	11'449'914
Rotor equivalent cell dimension, Δ_g	0.0628	0.0314	0.0157
Cells on the rotor	38	76	152
ε_{RMS}	0.028	0.028	0.032
Mean ε_{rel}	0.146	0.089	0.06

actuator line models, it is impossible to reach grid independence because of the coupling between the force projection width, ϵ and the mesh dimension. Thus, to select the characteristics of the grid to be used in the rest of the study, we use the experimental velocity profile at 2.3 rotor diameters downstream of the wind turbine. We run simulations on three different grids. The structural properties are the ones of the scaled model (carbon). The simulations are carried out with the same ϵ. The velocity profiles are normalized with respect to a reference velocity taken at hub height $1D$ upstream of the turbine.

Referring to Fig. 8, it is difficult to visually choose which model creates wake profiles best in agreement with the experiments. Therefore, the root mean square (RMS) of the absolute error between the computed and the measured wake profiles, and the relative error are taken to quantitatively describe the two models.

$$\varepsilon_{RMS} = \frac{\sqrt{\sum_{i=1}^{N}(U_{computed}^i - U_{measured}^i)^2}}{N} \tag{11}$$

where N is the number of locations at which the wake profile is measured.

$$\varepsilon_{rel} = \frac{U_{measured}^i - U_{computed}^i}{U_{measured}^i} \tag{12}$$

The wake error statistics are reported in Table 4. The intermediate and fine grids show a more symmetric profile, with the accelerated central region almost in line with the hub position (represented by the green dashed line in the center). The errors in this area are related to the fact that the nacelle has not been modeled in the simulations, so the flow is not decelerated.

The uniform Gaussian force distribution spreads the forces well beyond the blade tip and root, representing the blade longer than it is. For this reason, the numerical velocity profiles are more extensive than the experimental ones. We can also observe how the numerical simulations also over-predict the blade roots vortices. The description of the deficit in the root area is also affected by the fact that we are not modeling the nacelle. The coarse mesh over-predicts the velocity deficit, especially in the lower part, while the medium and fine grids are very close to the experimental values. The wind turbine performances are reported in Table 5. When constructing the fine mesh it was decided to limit the refined area to the near wake. Extending it to the end of the domain as in the other cases would have lead to a huge number of cells and unacceptable simulation times. Still, we went from one day an a half on the intermediate mesh to four days on the refined one. This choice limited the gain in accuracy that might have justified the additional effort. Therefore we decided to perform the rest of the study with a grid based on the intermediate one. This grid is described in Section 4.

Table 5

Rotor performances.

	Power [W]	$\Delta error\%$	Thrust [N]	$\Delta error\%$
Experiment	90.996		40.431	
Medium mesh				
$\epsilon = 2\Delta_g$	93.622	+2.89%	38.443	−4.92%
$\epsilon = 1.25\Delta_g$	97.639	+7.3%	38.803	−4.03%
Fine mesh				
$\epsilon = 2\Delta_g$	98.280	+8.04%	38.882	−3.83%
$\epsilon = 1.25\Delta_g$	109.395	+20.26%	40.111	−0.79%

Table 6

Blades construction materials.

Material	Mass density [g/cm^3]	Young Modulus [GPa]
Carbon fiber	1.7	220
E-glass	2.55	70

Table 7

Wind turbine operational parameters.

	V_{hub} [m/s]	ω [rpm]	λ_t	θ [deg]
Below Rated	3.71	241	8.07	0
Above Rated	5.03	265	6.24	12.5

5. Results

The two structural models described in Table 6 are simulated using OpenFAST BEM with ElastoDyn structural module. Intending to investigate the effect of different structural stiffness on the wind turbine wake flow, in addition to carbon fiber, we consider E-glass composite by changing the mass density and stiffness in the blade structural model. The tip out-of-plane deflection for the Elastic E-glass is 4.24% of the blade length as opposed to the 1.91% of the blade length we had with the elastic carbon. The flexibility obtained is enough to replicate the increasing size of future wind turbines and evaluate the effect of this variation on the wake flow. An additional simulation was performed with extreme flexibility under below rated conditions; obtaining a mean tip displacement of 12.1% of the blade length. It is an extreme case, very far from the previous ones and more points are necessary to conclude on a point where the advantage of using the coupling is higher than the cost. It should also be pointed out that at these deformation levels, the linear structural solver could encounter limitations due to the small displacement assumption it is based on. The wake evolution, structural response, and rotor performances are evaluated under the two wind conditions obtained with the precursor. The wind turbine operational parameters for the below-rated and above-rated conditions are reported in Table 7.

5.1. Below rated condition

Larsen et al. (2004) found that the effective rotor area changes with the blade deformations. These effects cause a reduction in power output under conditions between the cut-in and cut-out wind speeds. In contrast, the effects under the above-rated conditions are related to the pitch angle setting and control techniques. Fig. 9 shows the stream-wise mean velocity profiles at different positions downstream of the wind turbine. The velocity deficit and the recovery rate are underestimated within a turbulent flow field when the blade deformations are neglected. Significant variations are visible in the near wake up to 4D from the turbine and in the far wake at 8D. These effects are appreciable only when considering deflections above 4% of the blade length. Indeed the extreme flexible case has the more significant velocity deficit in the near wake and the lower in the far wake. At 6D, all the turbine configurations show a similar horizontal profile, but at 8D, the horizontal velocity deficit is lower for the two more flexible rotors. This behavior indicates that the recovery rate increases with the increase of blade elasticity. Fig. 10 shows the mean streamwise velocity difference from the rigid case in a horizontal plane passing through the hub center. With the increasing blade flexibility, velocities grow at the wake's outer edge and decrease at the center in the near wake. The wake recovery seems to start earlier for the rigid and carbon cases, but the recovery rate is faster for more elastic blades in the far wake.

The rotor performances are reported in Table 8 and illustrated in Fig. 11.

The resulting output values do not change very much for the rigid, Carbon, and E-glass cases. The effect of the flexibility on these parameters becomes essential only in the extreme elastic case. However, the trend already found in the literature (Larsen et al., 2004) is confirmed; the rotor performances decrease with the increase in blade tip deflections. Large deformations affect the wind turbine's power and thrust output due to the effective rotor area changes.

The structural deflections, flap-wise forces, and flap-wise moment are listed in Table 9. The mean flap-wise shear forces are little affected by the flexibility, while the range between maximum and minimum values decreases for more elastic blades. Also, the blade flap-wise root moments decrease along with the increasing elasticity.
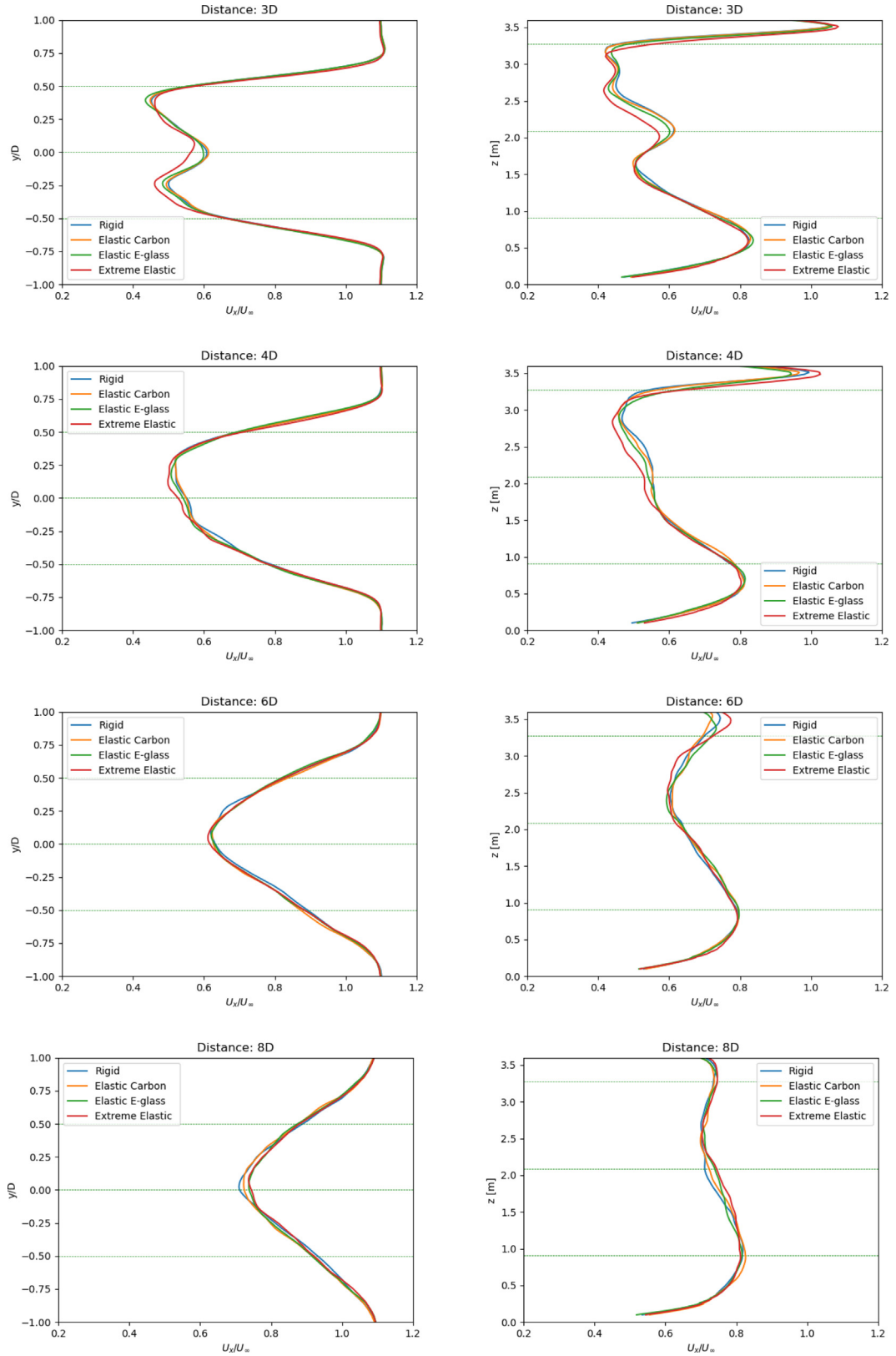
Fig. 9. Streamwise mean velocity horizontal profile (left) and vertical profile (right) at different distances downstream the turbine (below rated conditions).
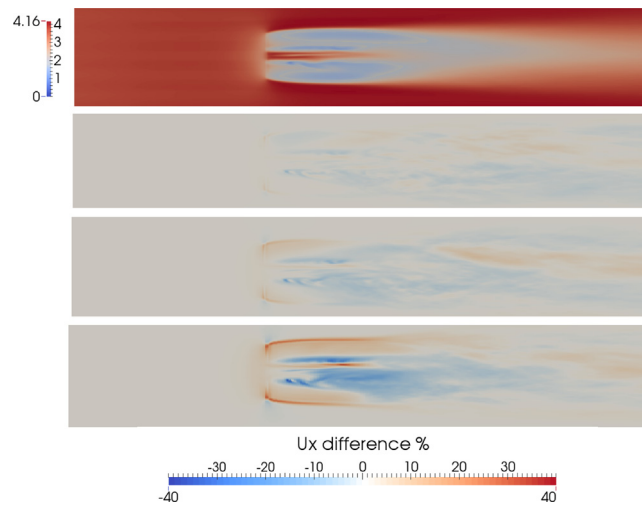
Fig. 10. Streamwise mean velocity contour - velocity difference with respect to the rigid case (top contour) on a horizontal plane passing through the hub center for Elastic Carbon, Elastic E-glass and Extreme Elastic (from top to bottom) for below rated conditions.
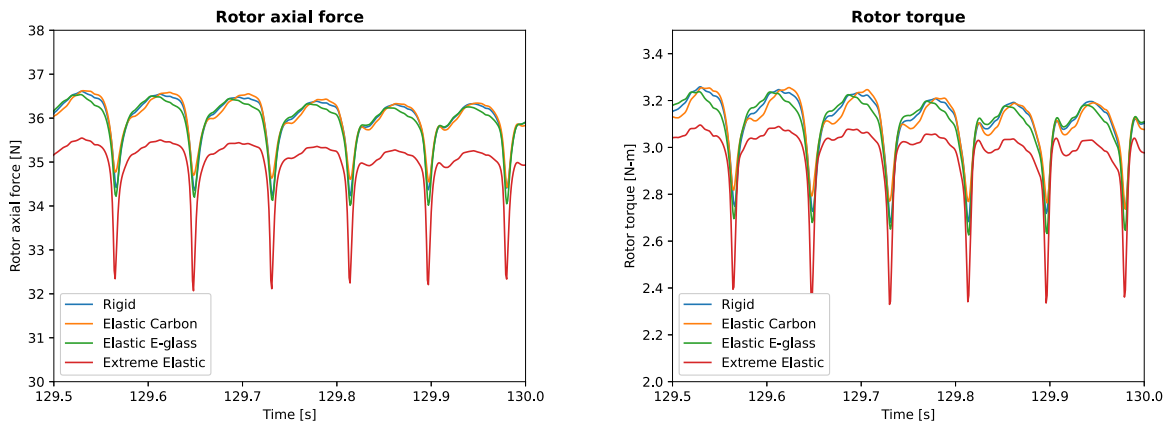

Fig. 11. Rotor performances - Below rated condition.

Table 8
Rotor performances below rated condition.

	Power [W]	Δ%[a]	Thrust [N]	Δ%[a]	Torque [N m]	Δ%[a]
Experiment[b]	74.468		37.432			
Rigid	78.322		36.118		3.103	
Elastic Carbon	78.200	−0.16%	36.123	+0.01%	3.099	−0.13%
Elastic E-glass	77.877	−0.57%	36.046	−0.20%	3.086	−0.55%
Extreme Elastic	74.706	−4.62%	35.082	−2.87%	2.960	−4.61%

[a]Difference with respect to the rigid configuration.
[b]Experimental data refers to a smooth wind tunnel condition.

5.2. Above rated condition

Ma et al. (2019) found that the underestimation of velocity and vorticity recovery rate becomes more pronounced with higher inlet velocities and more considerable tip deflections. Here, the pitch settings are set according to the values yielded from the controller used in the experimental tests. Therefore, the load and tip deflection are damped by pitch regulation techniques. The pitch angle used in this work is not the optimal value that would result from applying a controller directly to the simulated wind turbine. However, the effects of the variation are still visible. The resultant tip deformations are 1.75% and 3.79% of the blade length for the Carbon and E-glass rotors, respectively.
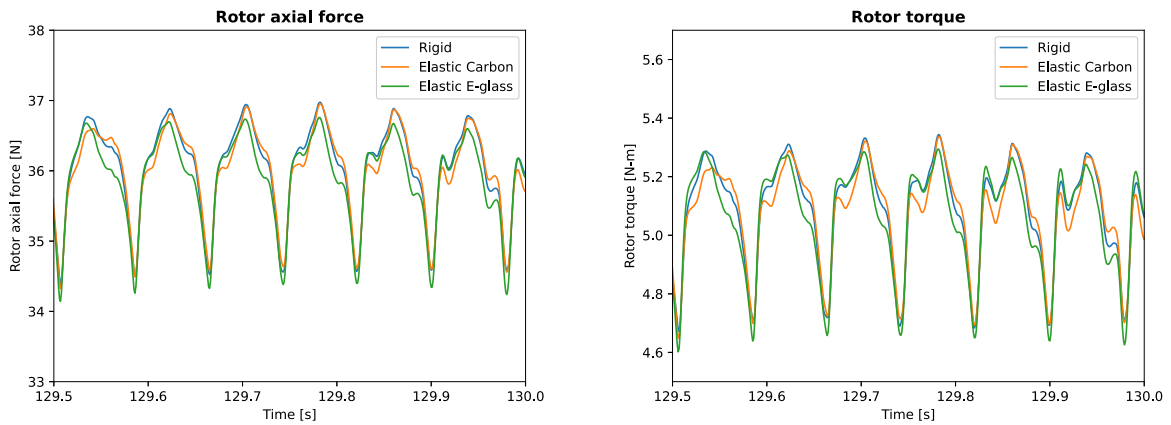
Fig. 12. Rotor performances - Above rated condition.

Table 9
Structural deformations, forces and moments (below rated conditions).

	Rigid	Elastic Carbon	Elastic E-glass	Extreme elastic
Tip Out-of-plane Deflection [m]				
Mean	0.0000	0.0226	0.0503	0.1435
% Blade R		1.91%	4.24%	12.11%
Maximum	0.0000	0.0261	0.0576	0.1529
Minimum	0.0000	0.0168	0.0394	0.1246
Blade Root Flapwise Shear Force [N]				
Mean	12.2	12.2	12.3	11.9
Maximum	12.9	14.3	13.8	12.9
Minimum	10.2	9.7	10.1	10.6
Blade Root Flapwise Moment [N m]				
Mean	9.1	8.5	7.3	5.0
Maximum	9.5	10.0	8.2	5.4
Minimum	7.5	6.6	5.8	4.4

Table 10
Rotor performances above rated condition.

	Power [W]	Δ%[a]	Thrust [N]	Δ%[a]	Torque [N m]	Δ%[a]
Experiment[b]	120.643		36.326			
Rigid	134.211		36.113		5.066	
Elastic Carbon	133.928	−0.21%	36.082	−0.09%	5.055	−0.22%
Elastic E-glass	133.188	−0.76%	35.945	−0.47%	5.027	−0.77%

[a]Difference with respect to the rigid configuration.
[b]Experimental data refers to a smooth wind tunnel condition.

These values are smaller than the low wind correspondent ones, meaning that the pitch regulation effectively reduces the blade deflections. The extreme elastic case was not analyzed for above rated conditions. Fig. 12 and Table 10 show the results in terms of performance.

Comparing Table 9 and 11, the flap-wise forces and moments are reduced passing from the below-rated to the above-rate conditions for the rigid, Carbon and E-glass cases. This means that pitch regulation is an efficient load alleviation method. Fig. 13 illustrates the wake deficit profile at different positions downstream of the turbine.

The horizontal and vertical profiles for the rigid, Carbon, and E-glass rotors are nearly identical both in shape and magnitude. The rotor performances are reported in Table 10. The power, thrust, and torque output are substantially the same for the three cases. The differences are in the temporal signals of these quantities shown in Fig. 12, where the flexibility slightly changes the peaks' shapes.
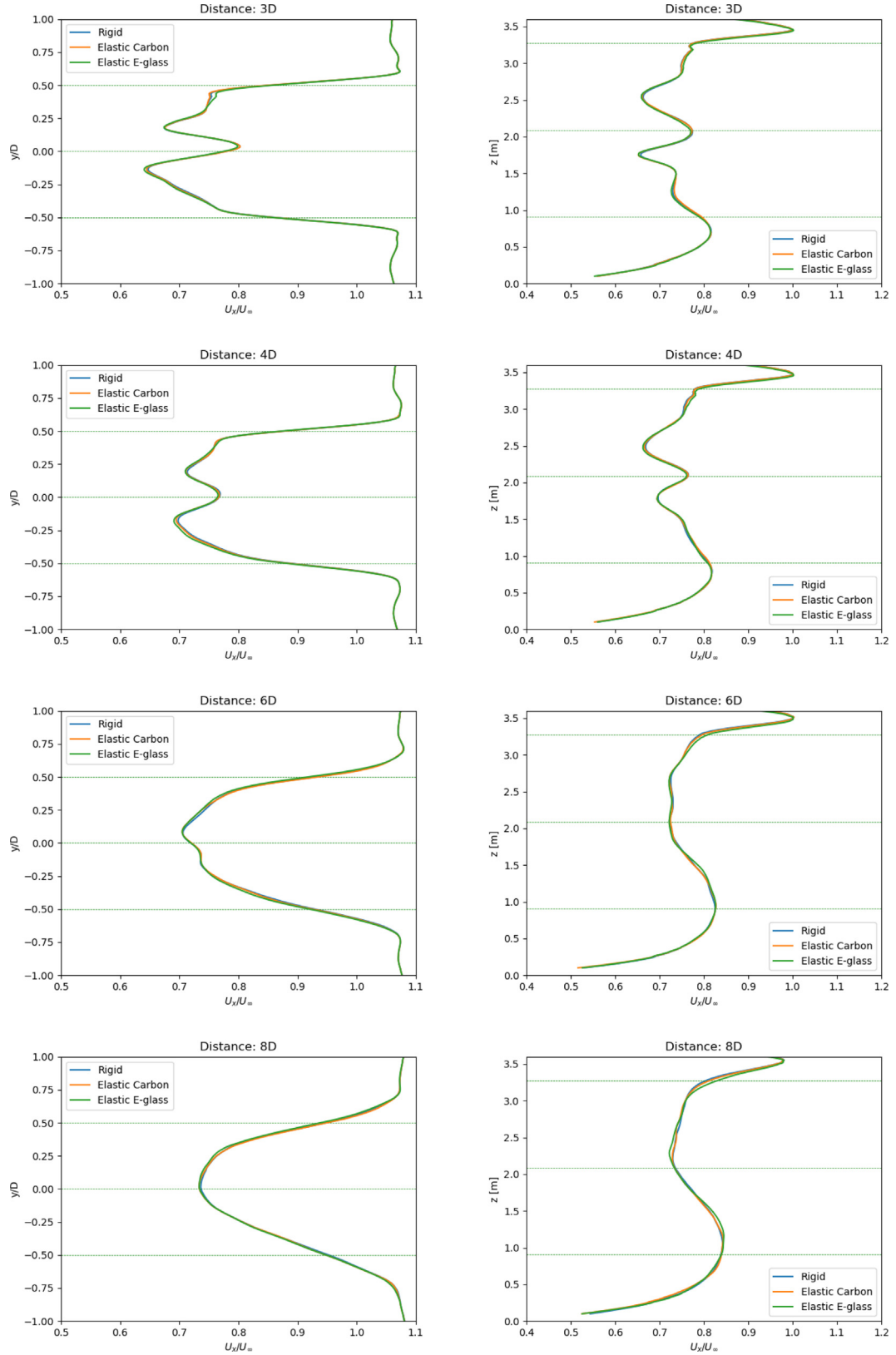
Fig. 13. Streamwise mean velocity horizontal profile (left) and vertical profile (right) at different distances downstream the turbine (above rated conditions).

Table 11
Structural deformations, forces and moments (above rated conditions).

	Rigid	Elastic Carbon	Elastic E-glass
Tip Out-of-plane Deflection [m]			
Mean	0.0000	0.0207	0.0449
% Blade R		1.75%	3.79%
Maximum	0.0000	0.0248	0.0558
Minimum	0.0000	0.0148	0.0304
Blade Root Flapwise Shear Force [N]			
Mean	12.4	12.4	12.5
Maximum	13.7	14.5	14.8
Minimum	9.5	9.2	9.0
Blade Root Flapwise Moment [N m]			
Mean	8.8	8.3	6.8
Maximum	9.6	9.8	8.2
Minimum	6.7	6.0	5.0

Table 12
Rotor performances. Below-rated linear vs non-linear.

	ElastoDyn	BeamDyn	Δ%
Power [W]	69.71	69.66	−0.1%
Thrust [N]	34.25	34.02	−0.7%
Torque [N m]	2.76	2.76	0%

Table 13
Structural deformations, forces and moments. Below-rated linear vs non-linear.

	ElastoDyn	BeamDyn	Δ%
Tip Out-of-plane Deflection [m]			
Mean	0.1208	0.1233	+2.1%
Maximum	0.1232	0.1253	+1.7%
Minimum	0.1185	0.1214	+2.4%
Blade Root Flapwise Shear Force [N]			
Mean	12.1	11.4	−5.8%
Maximum	11.7	11.6	−0.9%
Minimum	11.3	11.2	−0.9%
Blade Root Flapwise Moment [N m]			
Mean	8.0	7.9	−1.3%
Maximum	8.1	8.0	−1.2%
Minimum	7.9	7.8	−1.3%

5.3. Nonlinear effects

As mentioned in Section 2, the *BeamDyn* module is not yet integrated into the SOWFA-OpenFAST coupling. To have an idea of what exactly we are neglecting, we performed this analysis with the stand-alone OpenFAST software. The below-rated conditions and the standard material (carbon fiber) were considered. The smooth wind tunnel velocity profile is fed to OpenFAST through a tabulated velocity table.

The structural deflections, flap-wise forces and flap-wise moments are reported in Table 13. The tip deformations are underestimated when the non-linear effects are neglected. However, the difference is only 2% under low wind conditions. ElastoDyn slightly overpredicts the forces and moments, and the range between the maximum and minimum load peaks is greater than the BeamDyn one. The rotor performances are listed in Table 12. Power, Thrust, and Torque are nearly the same for the two solvers. On the other hand, the computational cost of the non-linear structural solver is much higher. The time step required for a stable solution is 0.001s for ElastoDyn and 0.00001s for BeamDyn. The resultant execution times are very different; BeamDyn requires several hours to simulate 35 s, while ElastoDyn computes that simulation time in a few minutes. Therefore, it can be concluded that a non-linear solver is unnecessary in a low wind condition of this type.

However, the main difference between the two structural solvers lies in the number of degrees of freedom computed. ElastoDyn does not consider the torsional deformation at all, which could be extremely important for control algorithms simulations. Indeed, the blade pitch angle would change due to this type of deformation.

Therefore, further investigations considering a complete description of the structural deformation are needed especially for above wind conditions, where the torsion effects are of primary importance for control purposes.

6. Conclusions

Wind turbines size is continuously increasing to extract more energy at a lower cost. However, larger rotors with enhanced flexibility increase aeroelastic effects that should be considered in an appropriate FSI framework. The simulation of the coupled aerodynamic and structural phenomena is a complex and computationally expensive task. Consequently, it is crucial to understand when it becomes strictly necessary. Using a CFD-CSD framework, we performed several simulations varying the turbine structural stiffness to get insight into the aeroelastic effects on the wake flow. In this research, we considered two typical operational conditions to evaluate these effects: below-rated and above-rated conditions.

Under the below-rated condition, for the Polimi DTU10MW model, the results show minor differences between the rigid and elastic simulation for both wake flow and turbine performances. The velocity deficit is underestimated if flexibility is neglected for tip deflection starting from 4% of the blade length. However, rotor performances show between variations of 0.20% for the thrust and 0.57% for the power. The differences become even more significant for tip displacement of 12%, yielding variations up to 2.87% for the thrust and 4.6% for the torque. Under the above-rated conditions, the effects are very similar considering a pitch-regulated wind turbine. For tip displacement around 4% the changes in rotor performances are between 0.47 and 0.77%. In conclusion, this study shows no need to perform coupled simulations when considering machines with tip deflections up to 4.2%.

These results should be confirmed experimentally, and further analysis should investigate higher tip deflections and account for non-linear effects properly.

CRediT authorship contribution statement

C. Muscari: Writing – original draft, Resources, Supervision, Data curation. **R. Giordani:** Formal analysis, Investigation, Data curation. **P. Schito:** Conceptualization, Resources, Supervision, Project administration.

Declaration of competing interest

The authors declare that they have no known competing financial interests or personal relationships that could have appeared to influence the work reported in this paper.

Data availability

Data will be made available on request.

References

Ahlström, A., 2006. Influence of wind turbine flexibility on loads and power production. Wind Energy Int. J. Progr. Appl. Wind Power Conversion Technol. 9 (3), 237–249.

Bak, C., Zahle, F., Bitsche, R., Kim, T., Yde, A., Henriksen, L.C., Hansen, M.H., Blasques, J.P.A.A., Gaunaa, M., Natarajan, A., 2013. The DTU 10-MW reference wind turbine. In: Danish Wind Power Research 2013.

Bayati, I., Belloli, M., Bernini, L., Boldrin, D., Boorsma, K., Caboni, M., Cormier, M., Mikkelsen, R., Lutz, T., Zasso, A., 2018. UNAFLOW project: UNsteady aerodynamics of floating wind turbines. In: J. Phys. Conf. Ser.. 1037, (7), IOP Publishing, 072037.

Bayati, I., Belloli, M., Bernini, L., Mikkelsen, R., Zasso, A., 2016. On the aero-elastic design of the DTU 10MW wind turbine blade for the LIFES50+ wind tunnel scale model. In: J. Phys. Conf. Ser.. 753, (2), IOP Publishing, 022028.

Churchfield, M., Lee, S., Moriarty, P., 2012. Overview of the simulator for wind farm application (SOWFA). Natl. Renew. Energy Lab..

Hansen, M.O.L., Sørensen, J.N., Voutsinas, S., Sørensen, N., Madsen, H.A., 2006. State of the art in wind turbine aerodynamics and aeroelasticity. Prog. Aerosp. Sci. 42 (4), 285–330.

Hsu, M.-C., Bazilevs, Y., 2012. Fluid–structure interaction modeling of wind turbines: simulating the full machine. Comput. Mech. 50 (6), 821–833.

Johlas, H., Martinez, L., Schmidt, D., Lackner, M., Churchfield, M.J., 2019. Large eddy simulations of floating offshore wind turbine wakes with coupled platform motion. Technical Report, National Renewable Energy Lab.(NREL), Golden, CO (United States).

Jonkman, J.M., 2003. Modeling of the UAE Wind Turbine for Refinement of FAST {_} AD. Technical Report, National Renewable Energy Lab., Golden, CO (US).

Jonkman, J.M., Buhl, M.L., et al., 2005. FAST User's Guide, vol. 365. National Renewable Energy Laboratory Golden, CO, USA.

Larsen, T.J., Hansen, A.M., Buhl, T., 2004. Aeroelastic effects of large blade deflections for wind turbines. Proc. Sci. Making Torque Wind 238–246.

Ma, Z., Zeng, P., Lei, L., 2019. Analysis of the coupled aeroelastic wake behavior of wind turbine. J. Fluids Struct. 84, 466–484.

Rodriguez, S.N., Jaworski, J.W., Michopoulos, J.G., 2021. Stability of helical vortex structures shed from flexible rotors. J. Fluids Struct. 104, 103279.

Sayed, M., Lutz, T., Krämer, E., Shayegan, S., Wüchner, R., 2019. Aeroelastic analysis of 10 MW wind turbine using CFD–CSD explicit FSI-coupling approach. J. Fluids Struct. 87, 354–377.

Shaler, K., Jonkman, J., 2021. FAST. Farm development and validation of structural load prediction against large eddy simulations. Wind Energy 24 (5), 428–449.

Shen, W.Z., Mikkelsen, R., Sørensen, J.N., Bak, C., 2005. Tip loss corrections for wind turbine computations. Wind Energy Int. J. Progr. Appl. Wind Power Convers. Technol. 8 (4), 457–475.

Sørensen, J.N., Shen, W.Z., 2002. Numerical modeling of wind turbine wakes. J. Fluids Eng. 124 (2), 393–399.

Yu, D.O., Kwon, O.J., 2014. Predicting wind turbine blade loads and aeroelastic response using a coupled CFD–CSD method. Renew. Energy 70, 184–196.